J. Fluid Mech. (1998), *vol.* 375, *pp.* 297–318. Printed in the United Kingdom

The measurement of the shear-induced particle and fluid tracer diffusivities in concentrated suspensions by a novel method

By VICTOR BREEDVELD[1], DIRK VAN DEN ENDE[1], ANUBHAV TRIPATHI[2] AND ANDREAS ACRIVOS[2]

[1]Twente Institute of Mechanics, J.M. Burgers center, Rheology Group, University of Twente, PO Box 217, 7500 AE Enschede, the Netherlands

[2]The Levich Institute, The City College of the City University of New York, New York, NY 10031, USA

(Received 9 February 1998 and in revised form 26 June 1998)

The shear-induced particle self-diffusivity in a concentrated suspension (20%–50% solids volume fraction) of non-colloidal spheres (90 μm average diameter) was measured using a new correlation technique. This method is based on the correlation between the positions of tracer particles in successive images and can be used to determine the self-diffusivity in non-colloidal suspensions for different time scales. These self-diffusivities were measured in the velocity gradient and vorticity directions in a narrow-gap Couette device for values of the strain $\gamma\,\Delta t$ ranging from 0.05 to 0.5, where γ is the applied shear rate and Δt is the correlation time. In both directions, the diffusive displacements scaled linearly with $\gamma\,\Delta t$ over the range given above and the corresponding diffusivities were found to be in good agreement with the experimental results of Leighton & Acrivos (1987*a*) and of Phan & Leighton (1993), even though these earlier studies were performed at much larger values of $\gamma\,\Delta t$. The self-diffusivity in the velocity gradient direction was found to be about 1.7 times larger than in the vorticity direction. The technique was also used to determine the shear-induced fluid tracer by measuring the mean square displacement of 31.5 μm diameter tracer particles dispersed in concentrated suspensions (30%–50% solids volume fraction) of much larger spheres (325 μm average diameter). These fluid diffusivities were found to be 0.7 times the corresponding particle diffusivities when both were scaled with $\gamma\,a^2$ ($2a = 325\,\mu$m).

1. Introduction

The self-diffusion of tracer particles in non-colloidal, as well as non-Brownian, suspensions has attracted a great deal of attention in recent years. Even at low Reynolds numbers, where inertial effects play a negligible role, particles in such suspensions exhibit diffusion-like motions due to hydrodynamic interactions with their neighbours whose positions have a random component. These interparticle interactions induce a net particle migration in the presence of inhomogeneities in the bulk shear rate or in the particle concentration.

In order to understand this self-diffusivity, consider a neutrally buoyant test sphere in a viscous suspension of otherwise identical spheres. When the suspension is subjected to an external shear flow, the test particle interacts with the other particles

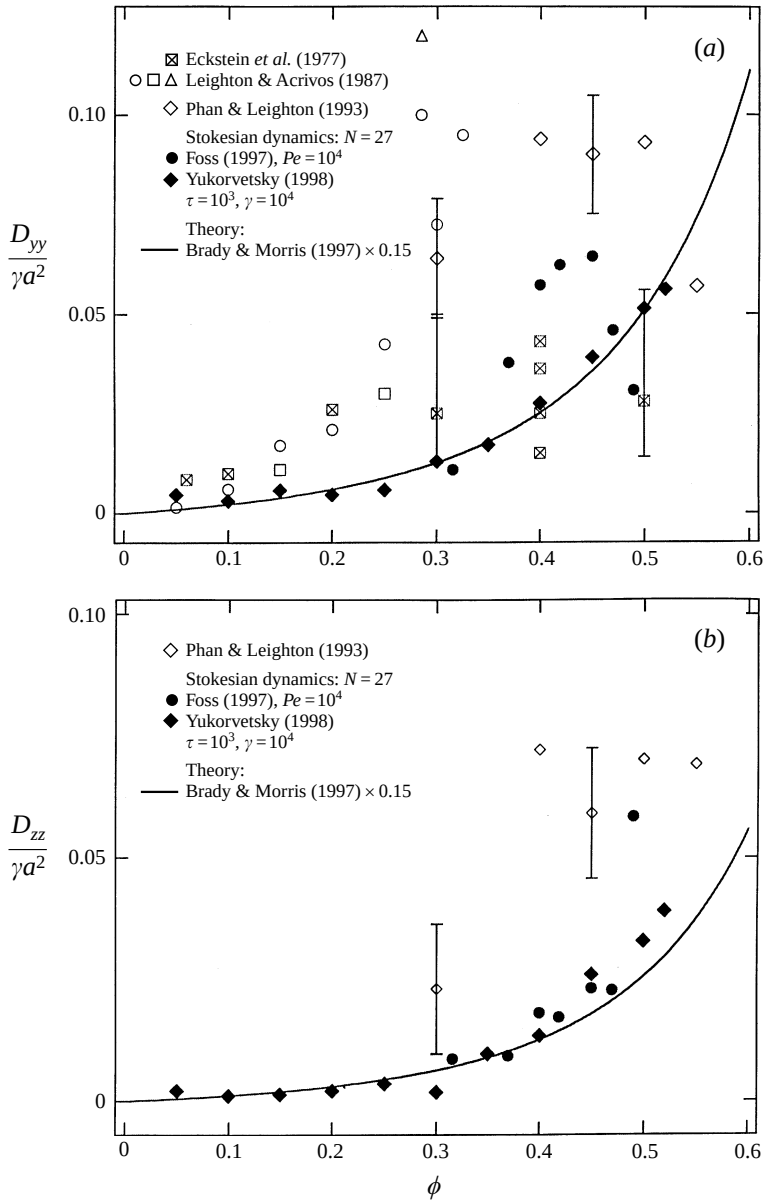

FIGURE 1. Data for the shear-induced self-diffusivity in a simple shear flow collected by Brady (1997) and plotted against the particle volume fraction in the suspension. (*a*) The self-diffusivity along the direction of shear; (*b*) the self-diffusivity along the vorticity axis. (Adapted with the permission of Professor J. F. Brady. The results of Foss (1997) are from a personal communication to Professor Brady.)

surrounding it and, consequently, experiences a series of displacements away from its original streamline. Such displacements, when taken together, will have zero mean but a finite mean square displacement which can be characterized by a shear-induced coefficient of self-diffusion. Since the rate of such interactions is proportional to the shear rate γ, and the length scale of each displacement is comparable to the particle radius a, the diffusion coefficient has a dimensional scaling γa^2 (Eckstein, Bailey & Shapiro

1977). It is important to note that the coefficient of self-diffusion associated with this mechanism is quite different from the shear-induced gradient diffusivity (Leighton & Acrivos 1987*b*), the latter being the coefficient in the linear relation between the particle flux resulting from a non-uniformity in the particle concentration and the concentration gradient. According to the arguments by Leighton & Acrivos (1987*b*), such a flux down a concentration gradient arises because a given particle in a sheared suspension experiences a greater number of interactions from the high concentration side than from the other. On the other hand, the mixing of marked spheres in a suspension of uniform concentration is entirely a self-diffusion process. Although this is one of the most basic transport processes occurring in sheared suspensions, only a few theoretical and experimental studies have been reported to date. These include the experimental measurements of the shear-induced self-diffusivity of non-Brownian particles by Eckstein *et al.* (1977), Leighton & Acrivos (1987*a*) and Phan & Leighton (1993), the computations via Stokesian Dynamics simulations by Bossis & Brady (1987), Phung, Brady & Bossis (1996), Phung (1993) and the theoretical work by Brady & Morris (1997). The results of all these studies are summarized in figure 1 (from Brady 1997) where the dimensionless self-diffusivities along the velocity gradient and vorticity directions are plotted as a function of the particle concentration ϕ. Clearly, owing to the large scatter in the experimental observations it is difficult to compare directly the experimental and computational results. In addition, in order to understand the nature of the microscopic interactions between the particles, measurements of the self-diffusivity over a wide range of values of the strain $\gamma\,\Delta t$, where Δt is the time step over which the particle displacement is observed, would be highly desirable. To our knowledge such measurements have not been attempted thus far.

Similarly, the self-diffusivity of a fluid tracer in non-colloidal concentrated suspensions has not been measured thus far in spite of its importance in many industrial and clinical processes. For example, a great deal of literature is available concerning liquid-phase mass transport in red blood cell suspensions and on the gas and heat transport in suspensions of particles. Zydney & Colton (1988) list about 50 publications on this topic. Although considerable evidence exists that both heat and mass transport in concentrated suspensions can be substantially augmented in shear flow, existing models are not completely adequate for predicting the experimental observations. We believe that the results of this study can be used to estimate the importance of augmented solute transport in the flow of concentrated suspensions, and also that they can provide a basis for a more detailed experimental and theoretical study of this phenomenon.

In this paper we shall present a new method for measuring the self-diffusion coefficient in concentrated suspensions of non-colloidal and non-Brownian particles. This technique is based on the application of spatial correlation procedures to consecutive images of tracer particles in a fixed imaging volume. In the next section, the general idea of the method will be explained, followed by the development of a theoretical framework for analysing the data. Then, in § 2.3 the theory will be applied to the case of a simple shear flow, applicable to the Couette geometry in which we performed our experiments. The third section contains a description of our experimental procedure and the final section is devoted to the results and discussion.

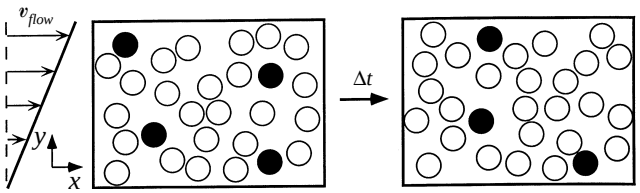

FIGURE 2. Schematic diagrams of two successive images of a fluid element in a sheared suspension.

2. The new approach

In this section we shall present the salient features of a simple and accurate experimental technique for measuring the self-diffusion coefficient in concentrated sheared suspensions.

2.1. *Basic concepts*

We examine the phenomenon of diffusion by investigating the positions of tracer neutrally buoyant spherical particles immersed in a suspension of otherwise identical spheres undergoing shear. The tracers are coloured black in order to distinguish them from the surrounding particles, which are refractive index matched with the suspending fluid. The images are taken at a fixed position in the geometry, but, because the suspension is being sheared, the tracers move with the general flow and will stay in the image window only for a limited time. Figure 2 shows an example of two successive images taken at a time interval Δt with the bulk flow as indicated so that all the particles move from left to right. The imaging window occupies a two-dimensional rectangular area. In an experimental set-up, the window will always be the two-dimensional projection of a three-dimensional fluid volume, because of the finite depth of focus of the optics (this effect will be dealt with in the next subsection and does not change the general considerations to be described below). The black particles in figure 2 represent the tracers, while the white ones refer to the refractive index matched particles, which are invisible if the matching is perfect. Particles intersecting the border of the image window are not drawn.

The motion of the non-colloidal particles consists of two parts: a convective motion along the streamlines of the bulk fluid flow and fluctuations due to their hydrodynamic interactions with other particles. The latter give rise to the shear-induced diffusion, both the self-diffusion and, if present, the gradient diffusion. An essential step in the technique consists of locating all the M tracers in the second image as well as all the N tracers in the first image and then calculating the two-dimensional vectors:

$$\Delta\tilde{\boldsymbol{x}}_{nm} = (x_m - x_n, y_m - y_n), \quad n = 1, 2, \ldots, N; m = 1, 2, \ldots, M,$$

where $(x_n y_n)$ and (x_m, y_m) refer to the positions of the particle centres in the first and second image, respectively. This results in $N \times M$ different two-dimensional displacement vectors $\Delta\tilde{\boldsymbol{x}}_{nm}$, generally a number too small for performing a meaningful statistical analysis. Figure 2, for example, yields 12 vectors. But if the procedure is repeated for a large number of image combinations with the same time interval, the number of vectors increases rapidly. These data can be used to define the function $C_{2D}(\Delta\tilde{\boldsymbol{x}}; \Delta t)$, which denotes the number of times a two-dimensional displacement vector $\Delta\tilde{\boldsymbol{x}}$ appears in the ensemble of images. The function $C_{2D}(\Delta\tilde{\boldsymbol{x}}; \Delta t)$ thus represents the experimental probability density of finding a vector $\Delta\tilde{\boldsymbol{x}}$ in the ensemble of images.

The vectors $\Delta\tilde{\boldsymbol{x}}_{nm}$ can be divided into two different categories. The first contains all the vectors $\Delta\tilde{\boldsymbol{x}}_{nm}^{auto}$ for which tracer m is the same as n. On these occasions, the

particle has not left the image window during the time interval. The second category contains all the cross-correlation vectors $\Delta\tilde{\boldsymbol{x}}_{nm}^{cross}$, between different tracer particles in consecutive images. For example, assume that N' ($N' \leqslant N$) particles in the first image of figure 2 are present in the second image as well. Then, the total number of $N \times M$ correlation vectors $\Delta\tilde{\boldsymbol{x}}_{nm}$ consists of N' auto-correlation vectors $\Delta\tilde{\boldsymbol{x}}_{nm}^{auto}$ and $N \times M - N'$ cross-correlation vectors $\Delta\tilde{\boldsymbol{x}}_{nm}^{cross}$. For the analysis of the particle motion, the auto-correlation vectors $\Delta\tilde{\boldsymbol{x}}_{nm}^{auto}$ are of interest because they contain information about the displacements of individual particles during the time interval Δt. The cross-correlation vectors are of less interest, although they contain information on the spatial distribution of the tracer particles in the fluid.

Unfortunately, it is impossible to tell *a priori* whether a vector $\Delta\tilde{\boldsymbol{x}}_{nm}$ belongs to the first or to the second category. This would only be possible if the time interval was very small, so that one could easily detect where the individual particles have gone. In the general case of larger time intervals, however, this would be very difficult and thus complicate the interpretation of the images. Fortunately, our technique does not need this information in evaluating the self-diffusivity. Specifically, we shall show in the next section that the auto-correlation and cross-correlation contributions to $C_{2D}(\Delta\tilde{\boldsymbol{x}};\Delta t)$ are of a different nature, and therefore can be separated statistically. Then, once the auto-correlation part has been extracted from the correlation vectors, the diffusive motion of individual particles can be analysed. Before proceeding though, let us first generalize the concept to the full three-dimensional formulation.

2.2. *Theoretical formulation in three dimensions*

In the experimental system, the two-dimensional images are the projection of a three-dimensional fluid volume. The effects of this projection onto a finite-sized two-dimensional image window have not been taken into account so far and will be analysed in this section. As will be shown, this slightly complicates the interpretation of the experimentally determined function $C_{2D}(\Delta\tilde{\boldsymbol{x}};\Delta t)$ mentioned in the previous subsection, but, after carefully considering these effects, $C_{2D}(\Delta\tilde{\boldsymbol{x}};\Delta t)$ can be directly related to the actual three-dimensional probability density of the particles which is the quantity of primary interest. No *a priori* assumptions on the nature of the particle motion have to be made.

The effect of the projection is that the three-dimensional vectors $\Delta\boldsymbol{x} \equiv (\Delta x, \Delta y, \Delta z)$ in the fluid volume become two-dimensional vectors $\Delta\tilde{\boldsymbol{x}} \equiv (\Delta x, \Delta y)$ on the image. Thus, in determining the function $C_{2D}(\Delta x, \Delta y;\Delta t)$ we are, in essence, counting the number of two-dimensional vectors $(\Delta x, \Delta y)$ appearing in the images by adding all the three-dimensional vectors $(\Delta x, \Delta y, \Delta z)$, regardless of the value of the out-of-plane distance Δz. This can be formulated mathematically as

$$C_{2D}(\Delta x, \Delta y;\Delta t) = \int C_{3D}(\Delta x, \Delta y, \Delta z;\Delta t)\mathrm{d}\Delta z, \tag{2.1}$$

where $C_{3D}(\Delta x, \Delta y, \Delta z;\Delta t)$ is the full three-dimensional spatial correlation probability of the ensemble of images, representing the chance of finding a displacement $(\Delta x, \Delta y, \Delta z)$. Off hand, it might appear that $C_{3D}(\Delta x, \Delta y, \Delta z;\Delta t)$ should equal $P(\Delta\boldsymbol{x};\Delta t,\boldsymbol{x})$, where $P(\Delta\boldsymbol{x};\Delta t,\boldsymbol{x})$ is defined as the theoretical probability density of finding two particles with centre-to-centre vector $\Delta\boldsymbol{x}$ after a given time interval Δt. However, owing to experimental limitations, the two functions are related by

$$C_{3D}(\Delta\boldsymbol{x};\Delta t) = \int\int\int_V S(\boldsymbol{x},\boldsymbol{x}+\Delta\boldsymbol{x})P(\Delta\boldsymbol{x};\Delta t,\boldsymbol{x})\mathrm{d}V, \tag{2.2}$$

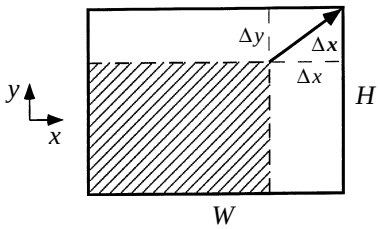

FIGURE 3. Schematic of the windowing effect on the correlation function for positive Δx and Δy.

where $S(\boldsymbol{x}, \boldsymbol{x}+\Delta\boldsymbol{x})$ to be discussed further on in this section is the experimental probability of detecting the particles referred to above.

The function $C_{3D}(\Delta x, \Delta y, \Delta z; \Delta t)$ thus represents the ensemble-averaged experimental sampling of the probability density $P(\Delta\boldsymbol{x}; \Delta t, \boldsymbol{x})$ and will be analysed in terms of $P(\Delta\boldsymbol{x}; \Delta t, \boldsymbol{x})$. Next, following the same arguments as in § 2.1, we split the probability density function $P(\Delta\boldsymbol{x}; \Delta t, \boldsymbol{x})$ into two parts. The first, termed the spatial auto-correlation in § 2.1, refers to the probability that the same particle has been displaced by $\Delta\boldsymbol{x}$. In terms of the probability distribution, it is equivalent to the transition probability density $P^{trans}(\Delta\boldsymbol{x}; \Delta t, \boldsymbol{x})$ of a particle being displaced by $\Delta\boldsymbol{x}$ during the time Δt, starting from position $\boldsymbol{x}$. The function $P^{trans}(\Delta\boldsymbol{x}; \Delta t, \boldsymbol{x})$ contains fundamental information on the particle motions.

The second contribution to the total probability density $P(\Delta\boldsymbol{x}; \Delta t, \boldsymbol{x})$ refers to the probability density of finding two different tracer particles at relative positions $\Delta\boldsymbol{x}$ after the time interval Δt. This part of the distribution probability density will be denoted by $P^{distr}(\Delta\boldsymbol{x}; \Delta t)$, since it is linked to the distribution of different tracer particles over the image window. $P^{distr}(\Delta\boldsymbol{x}; \Delta t)$ can then be expressed as

$$P^{distr}(\Delta\boldsymbol{x}; \Delta t) = \int\int\int P_1(\boldsymbol{x}) P_2(\boldsymbol{x}+\Delta\boldsymbol{x}; \Delta t : \boldsymbol{x}) \mathrm{d}\boldsymbol{x}, \tag{2.3}$$

where $P_1(\boldsymbol{x})$ is the probability density of finding a tracer at $\boldsymbol{x}$ and $P_2(\boldsymbol{x}+\Delta\boldsymbol{x}; \Delta t : \boldsymbol{x})$ is the conditional probability density of another tracer being at the position $\boldsymbol{x}+\Delta\boldsymbol{x}$ after a time interval Δt given that the first tracer was at $\boldsymbol{x}$. Also, the domain of integration is the whole image volume. Of course, if the tracers are distributed homogeneously over the window, P_1 is constant and can be taken out of the integration. Having thus defined the probability density functions $P^{trans}(\Delta\boldsymbol{x}; \Delta t, \boldsymbol{x})$ and $P^{distr}(\Delta\boldsymbol{x}; \Delta t)$, we proceed with the derivation of their relations with the spatial correlation function $C_{3D}(\Delta\boldsymbol{x}; \Delta t)$ (equation (2.2)), which in turn can be used to determine $C_{2D}(\Delta\tilde{\boldsymbol{x}}; \Delta t)$ via equation (2.1). The main effect to consider is the fact that the observed fluid volume is of limited size in all three directions and that the image analysis introduces some errors in detecting the particles in the images. Both factors influence the sampling function $C_{3D}(\Delta\boldsymbol{x}; \Delta t)$.

First, let us investigate the effect of the window boundaries in the x- and y-directions. Note that if the image window has width W and height H, the two-dimensional displacement vector $\Delta\tilde{\boldsymbol{x}}$ can never exceed the limits $-W < \Delta x < W$ and $-H < \Delta y < H$. As an extra complication, due to the limited size of the window, the chances of finding a large vector $(\Delta x, \Delta y)$ are lower than finding small ones. When both Δx and Δy are positive, this windowing effect is illustrated in figure 3 which shows that, within the fixed image window, the vector $(\Delta x, \Delta y)$ can only be realized starting from the shaded fraction of the window area, otherwise the end of the vector would point out of the window. Thus, the starting two-dimensional vector $\tilde{\boldsymbol{x}}$ must lie

inside the region bounded by

$$\tfrac{1}{2}(|\Delta x| - \Delta x) < x < W - \tfrac{1}{2}(|\Delta x| + \Delta x),$$
$$\tfrac{1}{2}(|\Delta y| - \Delta y) < y < H - \tfrac{1}{2}(|\Delta y| + \Delta y)$$

for the two-dimensional vector $\tilde{\boldsymbol{x}} + \Delta\tilde{\boldsymbol{x}}$ to be observed. The absolute values have to be used, because the windowing effect limits the effective size of the image window also for two-dimensional displacement vectors $\Delta\tilde{\boldsymbol{x}}$ with negative components.

In addition, it is not obvious that all the tracers within the fluid volume will be detected under all circumstances, as occurs, for example, when the lighting is inhomogeneous or when the tracers are too close together to be separated by both the human eye and sophisticated image analysis software. Therefore, it is reasonable to introduce the detection probability $S_{xy}(x, y)$ which varies over the image window. Ideally, when all the tracers can be detected, S_{xy} equals unity at all positions within the image window. Although this cannot be realized in practice, it is still possible to make S_{xy} almost a constant by carefully manipulating the lighting arrangement. But even so, its value will generally be slightly smaller than unity because, in any large collection of acquired images some of them will contain tracers that appear to be overlapping and cannot be located accurately.

The third dimension of the fluid volume is the z-direction, perpendicular to the object plane. Here, a finite volume around the focal plane of the optics will be observed due to the finite depth of focus (*d.o.f.*). Specifically, if $z = 0$ denotes the location of the focal plane, the depth of focus is usually defined so that the z-values at which tracer particles can be distinguished range from $-\frac{1}{2}d.o.f.$ to $+\frac{1}{2}d.o.f.$ As a result, the detection probability S_z will always be a very strong function of z. Even if we assume that S_z does not depend on the x- and y-positions (which is reasonable if the *d.o.f.* is small compared to the window size), it will, by definition, have its maximum in the focal plane and vanish at $z = \pm d.o.f.$ where the tracers can no longer be distinguished from their surroundings.

Using the arguments presented in the preceding paragraphs, equation (2.2) can be written in the following way:

$$\begin{aligned} C_{3D}(\Delta x, \Delta y, \Delta z; \Delta t) = & \int_{z_{min}}^{z_{max}} \int_{y_{min}}^{y_{max}} \int_{x_{min}}^{x_{max}} \left[\hat{n} S_{xy}(x, y) S_z(z) P_1(\boldsymbol{x})\right] \\ & \times \left[\hat{n} S_{xy}(x + \Delta x, y + \Delta y) S_z(z + \Delta z) P^{trans}(\Delta \boldsymbol{x}; \Delta t, \boldsymbol{x})\right] \mathrm{d}x\, \mathrm{d}y\, \mathrm{d}z \\ & + \int_{z_{min}}^{z_{max}} \int_{y_{min}}^{y_{max}} \int_{x_{min}}^{x_{max}} \left[\hat{n} S_{xy}(x, y) S_z(z) P_1(\boldsymbol{x})\right] \\ & \times \left[\hat{n} S_{xy}(x + \Delta x, y + \Delta y) S_z(z + \Delta z) P_2(\boldsymbol{x} + \Delta \boldsymbol{x}; \Delta t : \boldsymbol{x})\right] \mathrm{d}x\, \mathrm{d}y\, \mathrm{d}z, \end{aligned} \tag{2.4}$$

where

$$x_{min} = x_0 - \tfrac{1}{2}W + \tfrac{1}{2}(|\Delta x| - \Delta x),\ x_{max} = x_0 + \tfrac{1}{2}W - \tfrac{1}{2}(|\Delta x| + \Delta x),$$
$$y_{min} = y_0 - \tfrac{1}{2}H + \tfrac{1}{2}(|\Delta y| - \Delta y),\ y_{max} = y_0 + \tfrac{1}{2}H - \tfrac{1}{2}(|\Delta y| + \Delta y),$$
$$z_{min} = z_0 - \tfrac{1}{2}d.o.f. + \tfrac{1}{2}(|\Delta z| - \Delta z),\ z_{max} = z_0 + \tfrac{1}{2}d.o.f. - \tfrac{1}{2}(|\Delta z| + \Delta z)$$

and $\hat{n}$ is the average number of tracers in the fluid volume which is introduced in order to normalize the probability density functions. In addition, (x_0, y_0, z_0) denotes the centre of the object volume within which the measurements are being made. Both integrands in equation (2.4) involve a product of two terms: the first contains the

probability that a tracer is observed at position $\boldsymbol{x}$ and the second the probability that a tracer – either the same (P^{trans}) or another (P_2) – is observed at position $\boldsymbol{x}+\Delta\boldsymbol{x}$ after the time interval Δt. The integration over x, y and z originates from the finite size of the object volume, discussed earlier.

The general equation (2.4) can be simplified by letting $P_1(\boldsymbol{x})$ be constant, which is permissible if the gradients in the concentration of the tracer particles are negligible on the scale of the window size. In addition, as was stated earlier, $S_{xy}(x,y)$ will be constant under appropriate experimental conditions. Consequently, equation (2.4) becomes

$$C_{3D}(\Delta\boldsymbol{x};\Delta t) = K_1\,\hat{n}^2 \int_{z_{min}}^{z_{max}} \int_{y_{min}}^{y_{max}} \int_{x_{min}}^{x_{max}} S_z(z) S_z(z+\Delta z) P^{trans}(\Delta\boldsymbol{x};\Delta t,\boldsymbol{x})\,\mathrm{d}x\,\mathrm{d}y\,\mathrm{d}z + K_1\,\hat{n}^2 \int_{z_{min}}^{z_{max}} \int_{y_{aaaaaain}}^{y_{max}} \int_{x_{min}}^{x_{max}} S_z(z) S_z(z+\Delta z) P_2(\boldsymbol{x}+\Delta\boldsymbol{x};\Delta t:\boldsymbol{x})\,\mathrm{d}x\,\mathrm{d}y\,\mathrm{d}z, \tag{2.5}$$

where $K_1 = P_1 S_{xy}^2$ is an $O(1)$ constant. Therefore, on substituting equation (2.5) into equation (2.1) we obtain that

$$\begin{aligned} C_{2D}(\Delta\tilde{\boldsymbol{x}};\Delta t) &= K_1\,\hat{n}^2 \int_{-d.o.f.}^{+d.o.f.} \int_{z_{min}}^{z_{max}} \int_{y_{min}}^{y_{max}} \int_{x_{min}}^{x_{max}} S_z(z) S_z(z+\Delta z) P^{trans}(\Delta\boldsymbol{x};\Delta t,\boldsymbol{x})\,\mathrm{d}x\,\mathrm{d}y\,\mathrm{d}z\,\mathrm{d}\Delta z \\ &\quad + K_1\,\hat{n}^2 \int_{-d.o.f.}^{+d.o.f.} \int_{z_{min}}^{z_{max}} \int_{y_{min}}^{y_{max}} \int_{x_{min}}^{x_{max}} S_z(z) S_z(z+\Delta z) P_2(\boldsymbol{x}+\Delta\boldsymbol{x};\Delta t:\boldsymbol{x})\,\mathrm{d}x\,\mathrm{d}y\,\mathrm{d}z\,\mathrm{d}\Delta z, \end{aligned} \tag{2.6}$$

where the integration over Δz is performed from the minimum ($-d.o.f.$) to the maximum ($+d.o.f.$) possible distance between tracers in the Δz-direction. The second term on the right-hand side of equation (2.6) can be simplified further by considering special forms for $P_2(\boldsymbol{x}+\Delta\boldsymbol{x};\Delta t:\boldsymbol{x})$. Although some comments on this subject will be made at the end of the next subsection, a thorough analysis is beyond the scope of this paper, which concerns exclusively the first term. Note that, in arriving at equation (2.6), no *a priori* assumptions on the transition probability density $P^{trans}(\Delta\boldsymbol{x};\Delta t,\boldsymbol{x})$ have been made. In the next subsection, equation (2.6) will be evaluated when the transition probability is that for the diffusive motion of tracers in a simple shear flow, on which our experimental work is focused.

2.3. *The evaluation of self-diffusion coefficients in a simple shear flow*

The analysis discussed in the previous subsection directly links the experimental results to the transition probability density function of the tracers. Different theoretical hypotheses for $P^{trans}(\Delta\boldsymbol{x};\Delta t,\boldsymbol{x})$ can be introduced into equation (2.4) to check their validity. In this paper we concentrate on the topic of self-diffusion in a concentrated suspension undergoing simple shear flow. Previous experiments have shown that, for sufficiently long time steps Δt, the motion of the particles can be viewed as a diffusion process with different diffusion coefficients along the characteristic flow axes (flow, velocity gradient and vorticity direction). In such a case, the transition probability density $P^{trans}(\Delta\boldsymbol{x};\Delta t,\boldsymbol{x})$ satisfies the general convective diffusion equation:

$$\frac{\partial P^{trans}}{\partial t} = -\nabla\cdot(\boldsymbol{v}\,P^{trans}) + \nabla\cdot\boldsymbol{D}\cdot\nabla P^{trans} \tag{2.7}$$

with initial condition $P^{trans}(\Delta\boldsymbol{x};0,\boldsymbol{x}) = \delta(\Delta\boldsymbol{x})$, where $\boldsymbol{v}$ is the convective bulk particle velocity. For a stationary simple shear flow $\boldsymbol{v} = (\gamma y, 0, 0)$, with the x-axis in the flow direction and the y-axis in the velocity gradient direction. The diffusion tensor $\boldsymbol{D}$ is defined by

$$\langle \Delta\boldsymbol{x}\,\Delta\boldsymbol{x}\rangle \sim 2\,\boldsymbol{D}\Delta t = 2\begin{bmatrix} D_{xx} & D_{xy} & 0 \\ D_{yx} & D_{yy} & 0 \\ 0 & 0 & D_{zz} \end{bmatrix}\Delta t, \tag{2.8}$$

D_{xx}, D_{yy} and D_{zz} being the diffusion coefficients in the different directions. Due to symmetry, all the off-diagonal elements of $\boldsymbol{D}$ are zero except for D_{xy} and D_{yx} which are equal (cf. Brady & Morris 1997). The solution of equations (2.7) and (2.8) can be written in the form (cf. van Kampen 1992):

$$P^{trans}(\Delta\boldsymbol{x};\Delta t,\boldsymbol{x}) = \frac{1}{(2\pi)^{3/2}\sigma_x\sigma_y\sigma_z}\exp\left(-\frac{(\Delta x - \frac{1}{2}\gamma\Delta t(\Delta y + 2y) - \Delta y D_{xy}/D_{yy})^2}{2\sigma_x^2} - \frac{(\Delta y)^2}{2\sigma_y^2} - \frac{(\Delta z)^2}{2\sigma_z^2}\right), \tag{2.9}$$

where

$$\sigma_x^2 = 2D_{xx}\Delta t\left(1 + \frac{1}{12}\gamma^2\Delta t^2\frac{D_{yy}}{D_{xx}} - \frac{D_{xy}^2}{D_{xx}D_{yy}}\right), \quad \sigma_y^2 = 2D_{yy}\Delta t \ \text{ and } \ \sigma_z^2 = 2D_{zz}\Delta t.$$

On inserting equation (2.9) into equation (2.6) and integrating with respect to x, y and Δz, we obtain

$$\begin{aligned} C_{2D}(\Delta x,\Delta y;\Delta t) &= K_1\,\hat{n}^2\,\psi(\Delta t)\,\chi(\Delta t;dof)\,(W - |\Delta x|)\exp\left(-\frac{(\Delta y)^2}{2\sigma_y^2}\right) \\ &\quad\times\frac{\sqrt{\pi}\,\sigma_x}{\sqrt{2}\,\gamma\Delta t}\left(\operatorname{erf}\left[\frac{\Xi_1(\Delta x,\Delta y;\Delta t)}{\sqrt{2}\,\sigma_x}\right] - \operatorname{erf}\left[\frac{\Xi_2(\Delta x,\Delta y;\Delta t)}{\sqrt{2}\,\sigma_x}\right]\right) \\ &\quad + K_1\,\hat{n}^2\,(W - |\Delta x|)\,(H - |\Delta y|)\int_{-d.o.f.}^{d.o.f.}\int_{z_{min}}^{z_{max}} S_z(z)S_z(z+\Delta z)P_2(\Delta\boldsymbol{x};\Delta t{:}\,\boldsymbol{x})\,\mathrm{d}z\,\mathrm{d}\Delta z, \end{aligned} \tag{2.10}$$

where

$$\chi(\Delta t;d.o.f.) = \int_{-d.o.f.}^{d.o.f.}\int_{z_{min}}^{z_{max}} S_z(z)S_z(z+\Delta z)\,\exp\left(-\frac{(\Delta z)^2}{2\sigma_z^2}\right)\,\mathrm{d}z\,\mathrm{d}\Delta z. \tag{2.11}$$

$$\psi(\Delta t) = \frac{1}{(2\pi)^{3/2}\sigma_x\sigma_y\sigma_z}, \tag{2.12}$$

$$\Xi_1(\Delta x,\Delta y;\Delta t) = \Delta x - \tfrac{1}{2}\gamma\Delta t\left(2y_0 - H + |\Delta y|\right) - \Delta y\frac{D_{xy}}{D_{yy}}, \tag{2.13}$$

and

$$\Xi_2(\Delta x,\Delta y;\Delta t) = \Delta x - \tfrac{1}{2}\gamma\Delta t\left(2y_0 + H - |\Delta y|\right) - \Delta y\frac{D_{xy}}{D_{yy}}. \tag{2.14}$$

Equation (2.10) describes the shape of the experimentally determined function $C_{2D}(\Delta x,\Delta y;\Delta t)$ for the case of a diffusive tracer motion in a simple shear flow. As will

be shown in the more detailed description of the data analysis in § 3.3, this expression can be simplified further and then used to calculate the diffusion coefficient D_{yy} by analysing only the width of the auto-correlation peak of $C_{2D}(\Delta x, \Delta y; \Delta t)$ in the Δy-direction. Note that the amplitude of the auto-correlation part (first term) depends on the window size, the time step (through χ and ψ) and on the depth of focus of the optical system (through χ).

The preceding analysis can also be performed when the image plane is in the $(\Delta x, \Delta z)$-plane, which is the case when the suspension is viewed from the velocity gradient direction. Here, however, the counterpart of equation (2.10) is simply

$$\begin{aligned} &C_{2D}(\Delta x, \Delta z; \Delta t) \\ &= K_2\, \hat{n}^2\, \psi(\Delta t)\, \xi(\Delta x, \Delta t; d.o.f.)\, (W - |\Delta x|)\, (|H - \Delta z|)\, \exp\left(-\frac{(\Delta z)^2}{2\sigma_z^2}\right) \\ &\quad + K_2\, \hat{n}^2\, (W - |\Delta x|)\, (H - |\Delta z|) \int_{-d.o.f.}^{d.o.f.} \int_{y_{min}}^{y_{max}} S_y(y) S_y(y + \Delta y) P_2(\Delta \boldsymbol{x}; \Delta t : \boldsymbol{x})\, \mathrm{d}y\, \mathrm{d}\Delta y, \end{aligned} \tag{2.15}$$

where

$$\begin{aligned} \xi(\Delta x, \Delta t; d.o.f.) = &\int_{-d.o.f.}^{d.o.f.} \int_{y_{min}}^{y_{max}} S_y(y) S_y(y + \Delta y) \\ &\times \exp\left(-\frac{(\Delta x - \frac{1}{2}\gamma \Delta t(\Delta y + 2y) - \Delta y D_{xy}/D_{yy})^2}{2\sigma_x^2} - \frac{(\Delta y)^2}{2\sigma_y^2}\right) \mathrm{d}y\, \mathrm{d}\Delta y \end{aligned} \tag{2.16}$$

and $K_2 = P_1 S_{xz}^2$ is a constant which is slightly different from K_1. The above differs from equation (2.10) in the sense that the shape of the auto-correlation peak in the Δz-direction is simply that of a Gaussian peak, with a width that only depends on the diffusion coefficient D_{zz}. Consequently, equation (2.15) enables one to calculate the diffusion coefficient D_{zz} by analysing the width of the auto-correlation peak of $C_{2D}(\Delta x, \Delta y; \Delta t)$ in the Δz-direction. Equation (2.16) is somewhat more complicated than equation (2.11) because now ξ depends on both Δx and Δt.

Of course, the cross-correlation parts of equations (2.10) and (2.15) cannot be neglected in calculating the diffusion coefficients from the experimentally obtained functions C_{2D} because this part influences the shape of the correlation function in the region of the auto- correlation peak and must be subtracted out during the fitting procedures. To achieve this we recall that, as was mentioned in § 2.2, $P_2(\Delta \boldsymbol{x}; \Delta t)$ contains information about the distribution of different particles in consecutive images and is therefore closely related to the pair-distribution function. Symmetry arguments, therefore, are sufficient to eliminate the cross-correlation term in a simple shear flow. Specifically, as shown in figure 4, the $(\Delta x, \Delta y)$-plane on which our function is measured can be divided into four quadrants with the original position of the tracer being at the origin so that, in simple shear, the flow in quadrants II and IV is compressive and in quadrants I and III extensional. But, since the flow in quadrants I and III is equivalent and similarly in quadrants II and IV, the pair-distribution function has an obvious symmetry in that each point $A(\Delta x, \Delta y)$ has a counterpart $A'(-\Delta x, -\Delta y)$ where the pair-distribution function is the same. This symmetry should also apply to the function $P_2(\Delta \boldsymbol{x}; \Delta t)$ and, as will be shown in § 3.3, this argument enables one to eliminate the cross-correlation contribution from the measured experimental data in an elegant way.

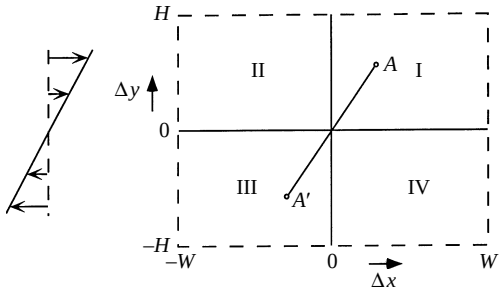

FIGURE 4. Schematic of four quadrants in the $(\Delta x, \Delta y)$-plane on which the function C_{2D} is measured. The origin refers to the original position of the tracer.

2.4. *Previous experimental work*

The general idea of the technique described above is in some respects similar to other well-known experimental methods, for example particle image velocimetry (PIV), where in order to measure the velocity field in complex flow geometries, the fluid is seeded with small tracers which accurately follow the flow because of their small size. One difference, however, is that, whereas PIV uses very small time intervals Δt between the images to calculate velocity vectors, the time intervals are considerably larger in the present application so as to maximize the displacements of the tracers.

On the other hand, Eckstein *et al.* (1977) and Leighton & Acrivos (1987*a*) examined the phenomenon of self-diffusion by investigating the motion of a single labelled sphere immersed in a suspension of otherwise identical spheres being sheared in a Couette device. In their technique, the radial position (the velocity gradient direction) of the labelled sphere was measured after each rotation (Eckstein *et al.*) or inferred from the time taken for the particle to complete a transit of the device (Leighton & Acrivos). These data were then related to the random walk in the radial direction. Recently, Phan & Leighton (1993) also measured the self-diffusivity in the vorticity direction by observing the vertical position of a marked sphere each time it passed an observation window. It is worth remarking at this point that in the experiments of both Leighton & Acrivos (1987*a*) and Phan & Leighton (1993), the strain $\gamma \Delta t$ was at least of $O(10)$, which, as will be shown presently, is more than an order of magnitude larger than in our experiments.

3. Experimental work

In this section we present the experimental details of our measurements of the shear-induced coefficient of particle self-diffusion. The basic approach consisted of evaluating the positions of tracer particles, immersed in a suspension of otherwise identical spheres, being sheared in a narrow-gap Couette device.

3.1. *Apparatus and materials*

The experiments were performed in a narrow-gap cylindrical Couette device, shown in figure 5, which consisted of two cylinders made of high quality Plexiglas. The inner radius of the outer stationary cylinder (R_O) was 8.224 cm and the outer radius of the inner rotating cylinder (R_I) was 7.542 cm, giving a gap size equal to 0.682 cm. The inner cylinder was mounted on a shaft, which in turn was mounted on a computer controlled feedback motor (ID Corp., California). Also, the shaft was aligned accurately with two bearings separated by O-rings. A great advantage of this

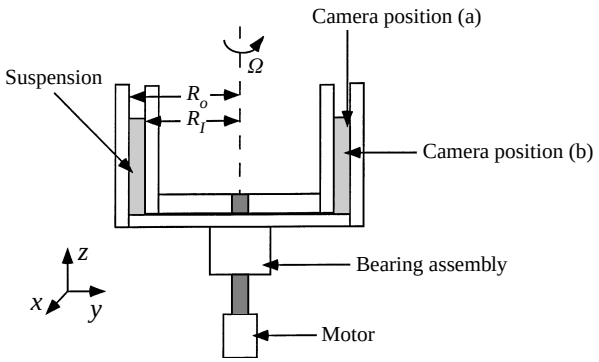

FIGURE 5. Schematic of the Couette device and the camera positions (a) and (b) for observations in, respectively, the velocity gradient and vorticity directions.

design is that its transparency enabled us to provide uniform lighting to the imaging volume.

The particles used in the experiments were class 4F acrylic spheres obtained from ICI. Their density was measured to be 1.172 g ml^{-1} and the spheres containing air bubbles were removed by density segregation. The polydisperse material was sieved many times to obtain the diameter range $90 \pm 15\mu m$. Following the recipe of Krishnan, Beimfohr & Leighton (1996), a suspension of these particles was made using a mixture of 77.38% Triton X-100, 9.23% water and 13.39% anhydrous zinc chloride (weight percentages) which matched the refractive index and density of the acrylic spheres. The pure suspending fluid had a viscosity of 3.4 Pa s at the operating temperature of 23°C. Tracer particles were prepared by dyeing part of the acrylic spheres with RIT liquid fabric dye and their density was also found to be close to 1.172 g ml^{-1}. A small amount of the tracer particles (typically 0.4 vol.% in our experiments) was then added to the suspension. The suspension was sheared for several hours to achieve a uniform concentration and to drive out any air bubbles. The experiments were carried out at two shear rates (0.78 s^{-1} and 1.8 s^{-1}) for particle volume fractions of 20%, 30%, 40% and 50%.

3.2. *Image analysis*

The motion of the tracer particles was observed by viewing two small volumes of the suspension from positions (a) and (b), shown in figure 5, using a high resolution (1008 × 1018 pixels) CCD camera (Kodak MegaPlus ES1.0) with Infinity Optics (8× magnification). For lighting we used a Fiber Optic Illuminator (Cole Parmer Instrument Company) that provided an excellent contrast in the image. The camera was mounted on a three-dimensional traversing system, which allowed us to focus the camera precisely at the desired locations. Images from the CCD camera were passed via an 8-bit digital video signal to a dedicated image acquisition and processing board (Oculus F64 by Coreco Inc.) which operated on a personal computer equipped with a 200 MHz Intel Pentium Processor. We programmed the frame buffer arrays of the F64 board to enable the acquisition of 5 consecutive images at equal time intervals Δt (with $\Delta t_{min} = 55$ ms) before storing the images into the hard disk of the computer. This program was typically run with 100 loops to acquire and store 500 images automatically. The grabbing times of all the images were stored for further analysis.

We used the positions (a) and (b), shown in figure 5, to measure the self-diffusion coefficients in the velocity gradient and in the vorticity directions respectively. When

viewing from position (a), the centre of the imaging volume was kept at 1 mm below the top interface and at 1.5 mm inside the outer wall of the Couette gap, while when viewing from position (b) the centre of the fluid element $W \times H \times d.o.f.$ of the suspension was chosen 1.7 cm above the bottom and 1 mm inside the outer wall of the Couette gap. These positions were chosen to reduce the wall effects as far as possible. The cross-sectional area, $W \times H$, was calculated using the known magnification of the camera optics and in our experiments was found to be 1.17 mm $\times$ 1.18 mm. The depth of focus, *d.o.f.*, was determined by viewing a 45° inclined plane through the camera with the preset optics. The inclined plane had four sets of target columns containing different numbers of line pairs per millimetre. The resolution appropriate for the given magnification was then chosen and the distance up to which the line pairs were distinctly visible was measured. This distance was read from either the computer monitor or the scale on the inclined plane. Using this technique, the depth of focus was found to be 425 ± 25 μm.

The positions of the tracer particles in each digitized image were accurately determined using the imaging software (Visilog 5.1 by Noesis Vision Inc.). This software stretched the pixel-grey value dynamic range (process called equalization) to make the details more visible and then removed the unwanted small-scale noise. After running a binarization operation, border particles were eliminated and analysis procedures were performed on the dark objects in the image. These procedures involved the calculation of the areas, sphericities, blackness and positions of the dark objects. If the properties met our pre-set criteria, an object was counted as being a tracer and the position of its centre was stored in a file. In this way, all the images were scanned and all the tracers and their locations were identified.

For our self-diffusion measurements, a large number of images were taken for each run in order to ensure good ensemble averaging. Typically, we acquired 500 images. The positions of the tracers, as obtained from the measurements described above, were then used to generate the correlation functions C_{2D} for each set. The method for generating these functions and evaluating the self-diffusion coefficients will now be described.

3.3. *Data analysis*

The data on the positions of all the tracer particles in the images were used to calculate the correlation function $C_{2D}(\Delta x, \Delta y; \Delta t)$ in the following way. For the total ensemble, the two-dimensional displacement vectors $(\Delta x_{nm}, \Delta y_{nm})$ were calculated for all combinations of the tracers in consecutive images, as described in § 2.1. The $(\Delta x, \Delta y)$-domain ($-W \leqslant \Delta x \leqslant W$ and $-H \leqslant \Delta y \leqslant H$) was discretized in $N_{\Delta}x \times N_{\Delta y}$ small area elements, usually called numerical bins. All the vectors $(\Delta x_{nm}, \Delta y_{nm})$ were put into the corresponding numerical bin. The number of vectors in each bin was then divided by the number of images, N_{ima}, and by the area covered by each numerical bin, $(2W/N_{\Delta x})(2H/N_{\Delta y})$, to arrive at the normalized value of the correlation function $C_{2D}(\Delta x, \Delta y; \Delta t)$ at the position of the centre of the bin. The normalization procedure is necessary to obtain the correct value if numerical integration is performed and to allow comparison with the theoretical predictions of equations (2.10) and (2.15). The number of bins $N_{\Delta x} \times N_{\Delta y}$ must be small enough in order for each bin to contain a sufficient number of vectors for further analysis, but large enough to provide information on the behaviour of the correlation function at small length scales.

From each ensemble of images, the correlation function could be obtained for different time steps, by not only comparing consecutive images at a time interval Δt,

but by also analysing image combinations at other intervals $(2\Delta t, 3\Delta t)$ within one grabbing sequence of five images.

Using the data analysis procedures described above, three-dimensional plots could be generated of the function $C_{2D}(\Delta x, \Delta y; \Delta t)$ on the $(\Delta x, \Delta y)$-plane. Because in our experimental set-up the particles moved from left to right due to convection, the auto-correlation peak in equations (2.10) and (2.15) was always located at positive values of Δx. As a result, the values of the correlation function $C_{2D}(\Delta x, \Delta y; \Delta t)$ for $\Delta x > 0$ involve a combination of an auto- and a cross-correlation, whereas the values of $C_{2D}(\Delta x, \Delta y; \Delta t)$ for $\Delta x < 0$ consist only of cross-correlation contributions. Using the symmetry argument presented in § 2.3, the auto-correlation part of $C_{2D}(\Delta x, \Delta y; \Delta t)$ can then be obtained by calculating

$$C_{2D}^{auto}(\Delta x, \Delta y; \Delta t) = C_{2D}(\Delta x, \Delta y; \Delta t) - C_{2D}(-\Delta x, -\Delta y; \Delta t) \quad for\ \Delta x \geqslant 0. \tag{3.1}$$

In order to evaluate the diffusion coefficients we focused our quantitative analysis on the displacements Δy in the velocity gradient (and Δz in the vorticity direction). Since we are not interested in the Δx-displacements, we used a very small number of bins in Δx, $N_{\Delta x} = 2$, i.e. one for negative and one for positive Δx-values. Then, after performing the subtraction of equation (3.1), we integrated $C_{2D}^{auto}(\Delta x, \Delta y; \Delta t)$ over Δx to obtain (see equation (2.10))

$$C_{1D}^{auto}(\Delta y; \Delta t) = A \exp\left(-\frac{(\Delta y)^2}{2\sigma_y^2}\right) \tag{3.2}$$

with

$$A = K_1\, \hat{n}^2\, \psi(\Delta t)\, \chi(\Delta t; d.o.f.)\, \frac{\pi^{1/2}\, \sigma_x}{\sqrt{2}\, \gamma \Delta t} \times \int_{-W}^{W} (W - |\Delta x|) \left(\operatorname{erf}\left[\frac{\Xi_1(\Delta x, \Delta y; \Delta t)}{\sqrt{2}\, \sigma_x}\right] - \operatorname{erf}\left[\frac{\Xi_2(\Delta x, \Delta y; \Delta t)}{\sqrt{2}\, \sigma_x}\right] \right) \mathrm{d}\Delta x.$$

In principle, as seen from the above, Δy should also enter into the expression for the amplitude A in view of equations (2.13) and (2.14) thereby complicating the data analysis. But since $|\Delta y|$ is of the order of the particle radius a (and, similarly, for $\Delta y D_{xy}/D_{yy}$ provided that D_{xy}/D_{yy} is $O(1)$ or smaller), while H, y_0 and W are all $O(1\ \mathrm{mm})$ and therefore an order of magnitude larger, the amplitude A becomes independent of $|\Delta y|$ with an error of $O(a/H)$. Consequently, the width of the peak of C_{1D}^{auto} determines σ_y^2 which, in view of equation (2.9), equals twice the product of D_{yy} with the time interval Δt, so that the diffusion coefficient can be determined by fitting the experimental data with equation (3.2).

We followed a similar procedure for analysing the function $C_{2D}(\Delta x, \Delta z; \Delta t)$ and calculating the diffusivity D_{zz} in the vorticity direction. Again, after subtracting the cross-correlation part, we integrated $C_{2D}^{auto}(\Delta x, \Delta z; \Delta t)$ over Δx to obtain (see equation (2.15))

$$C_{1D}^{auto}(\Delta z; \Delta t) = B(H - |\Delta z|) \exp\left(-\frac{(\Delta z)^2}{2\sigma_z^2}\right) \tag{3.3}$$

with

$$B = K_2\, \hat{n}^2\, \psi(\Delta t) \int_{-W}^{W} \xi(\Delta x, \Delta t; d.o.f.)\, (W - |\Delta x|)\, \mathrm{d}\Delta x.$$

As $H \gg |\Delta z|$, the square of the width σ_z of this peak equals twice the product of

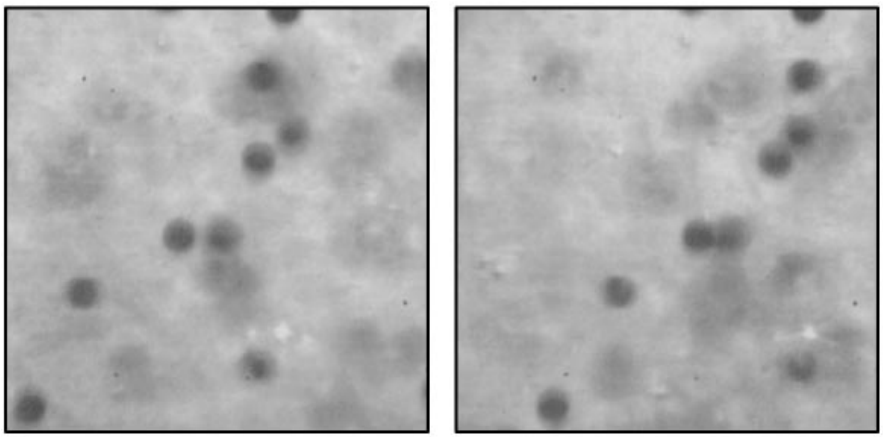

FIGURE 6. Photographs of two succesive images taken 220 ms apart in a 30% concentrated suspension sheared at 1.79 s^{-1}. Here, the flow is from left to right.

the diffusion coefficient D_{zz} and the time interval Δt (see also equation (2.9)). Hence the diffusion coefficient D_{zz} can be determined by fitting the experimental data with equation (3.3).

In summary then, the diffusion coefficients D_{yy} and D_{zz} can be calculated by reducing the two-dimensional correlation functions $C_{2D}(\Delta x, \Delta y; \Delta t)$ and $C_{2D}(\Delta x, \Delta z; \Delta t)$ to the functions $C_{1D}(\Delta y; \Delta t)$ and $C_{1D}(\Delta z; \Delta t)$, respectively, and by subsequently fitting the resulting curves with the Gaussian peaks of equation (3.2) and (3.3). The amplitudes A and B of the respective equations (3.2) and (3.3) peaks were not analysed thoroughly, because they contain a number of unknown functions.

4. Results and discussion

4.1. *Validation of the technique*

Using the experimental set-up, images were obtained of sufficiently high quality to carry out the required accurate image analysis procedures. A typical example of our image quality is shown in figure 6, which depicts a sample of two consecutive images ($\Delta t = 220$ ms) in a suspension with particle concentration $\phi = 0.30$ being sheared at the rate $\gamma = 1.79\ s^{-1}$.

In order to ensure that any observed self-diffusivity in a concentrated suspension was due only to the diffusive motion of the tracers, it was necessary to rule out the existence of any significant errors in our experimental set-up or in the image analysis procedure. The possible errors in the former included mechanical vibrations, rotation irregularities of the motor, non-uniformities in the Couette gap and misalignment of camera-optics. In addition, we expected some error in the calculation of the particle locations by the image analysis procedure. Although the importance of the image analysis error could not be estimated *a priori*, the errors originating from this source were minimized by applying homogeneous lighting and optimizing the contrast.

In order to quantify these errors, we performed measurements in a dilute suspension ($\phi = 0.4\%$) of only tracer particles, where the self-diffusivity was expected to be negligible compared to the self-diffusivities reported in the literature for concentrated suspensions. Following the procedures described in § 3, the broadening of the

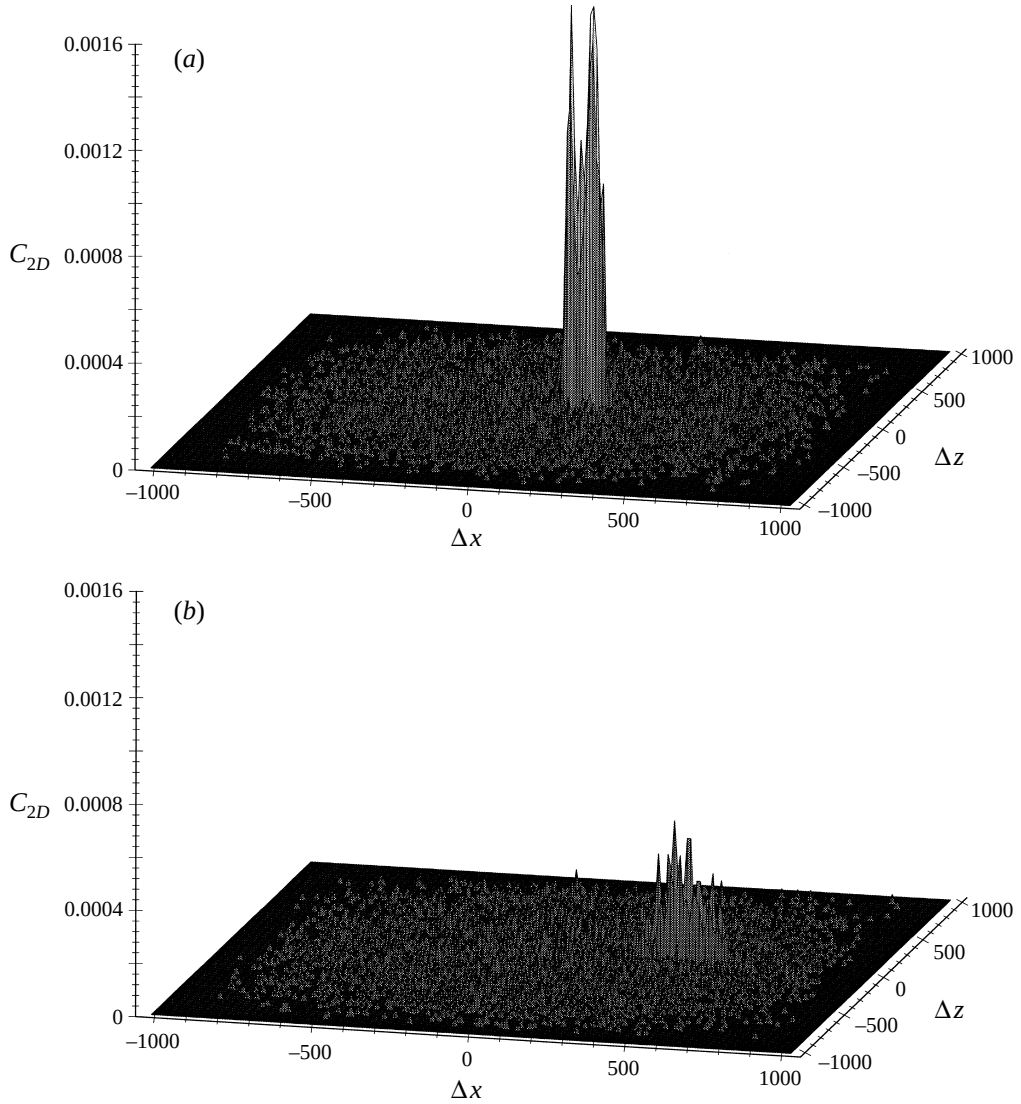

FIGURE 7. Plots of the experimentally determined correlation function C_{2D} in the $(\Delta x, \Delta z)$-plane for $\phi = 0.30$ and (*a*) $\gamma\,\Delta t = 0.085$, (*b*) 0.34.

correlation peaks in both the velocity gradient and vorticity direction was measured. This broadening is believed to be the result of the systematic errors mentioned above. If it was interpreted as self-diffusion, we found that the value of the associated diffusion coefficient was at most 10% of the values we observed for the concentrated suspensions at 30% volume fraction. The influence of the image analysis procedures on the diffusivity results was also checked and the results were found to be insensitive to changes in the criteria which we used for the detection of tracer particles in the images. These measurements in the dilute suspension showed that the contributions of the experimental errors were small. Hence, we applied the technique to determine the self-diffusivity in concentrated suspensions.

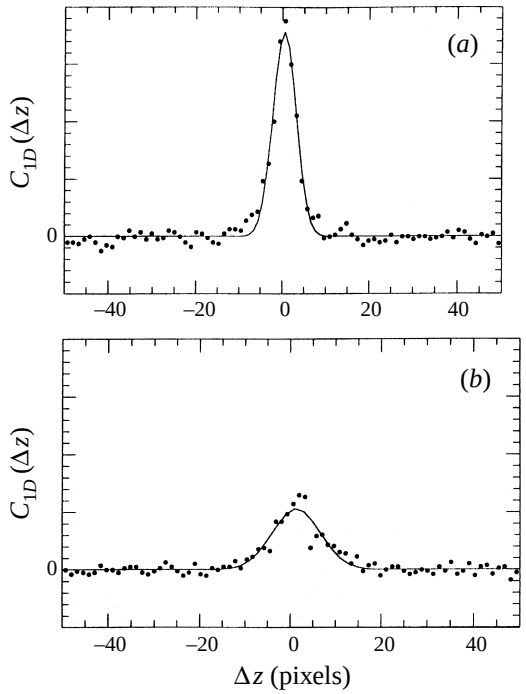

FIGURE 8. Plots of the experimentally determined correlation function C_{1D} vs. the displacement Δz for $\phi = 0.30$ and (*a*) $\gamma\,\Delta t = 0.085$ (*b*) 0.34.

4.2. *Particle self-diffusion in concentrated suspensions*

The diffusion-coefficient experiments were conducted at solids concentrations ranging from 20% to 50% for values of $\gamma\Delta t$ ranging from 0.05 to 0.5.

In figure 7 we present three-dimensional correlation plots for the case of $\phi = 0.30$ at $\gamma\Delta t = 0.085$ and 0.34, where $C_{2D}(\Delta x, \Delta z\,; \Delta t)$ is shown as a function on the $(\Delta x, \Delta z)$-plane according to the analysis procedures described in § 3.2. The Δx- and Δz-axes respectively represent the correlation distances in the velocity and vorticity gradient direction. The units of the displacements in the figures are pixels, for direct reference to the images. The auto-correlation peak is clearly distinguishable and is dominant over the cross-correlation contribution, which appears as the scatter in the rest of the plane. The width in the Δx-direction is the result of variations in the convective velocity over the window (see figure 2); in the Δz-direction the width is governed by the diffusive process and is much smaller. As the time step Δt increases – from figure 7(*a*) to 7(*b*) –, the convective displacements increase and the peak shifts to the right. Also, the amplitude of the peak decreases, as fewer particles are detected in two consecutive images. These observations are in qualitative agreement with our expectations and figure 7 further validated our choice of the number of images acquired per run and the time interval Δt between consecutive images.

For a quantitative analysis, the three-dimensional plots of figure 7 were reduced to plots of $C_{1D}(\Delta z\,; \Delta t)$ as discussed in § 3.3. Figure 8 shows the graphs of $C_{1D}(\Delta z\,; \Delta t)$ versus Δz for the same experimental data as presented in figure 7, after subtraction of the cross-correlation part. Again, the displacements are expressed in pixels, but this could easily be transformed into SI-units by using the known camera magnification (1 pixel = 1.16 μm). The graphs also show the best possible fit with a Gaussian peak. It

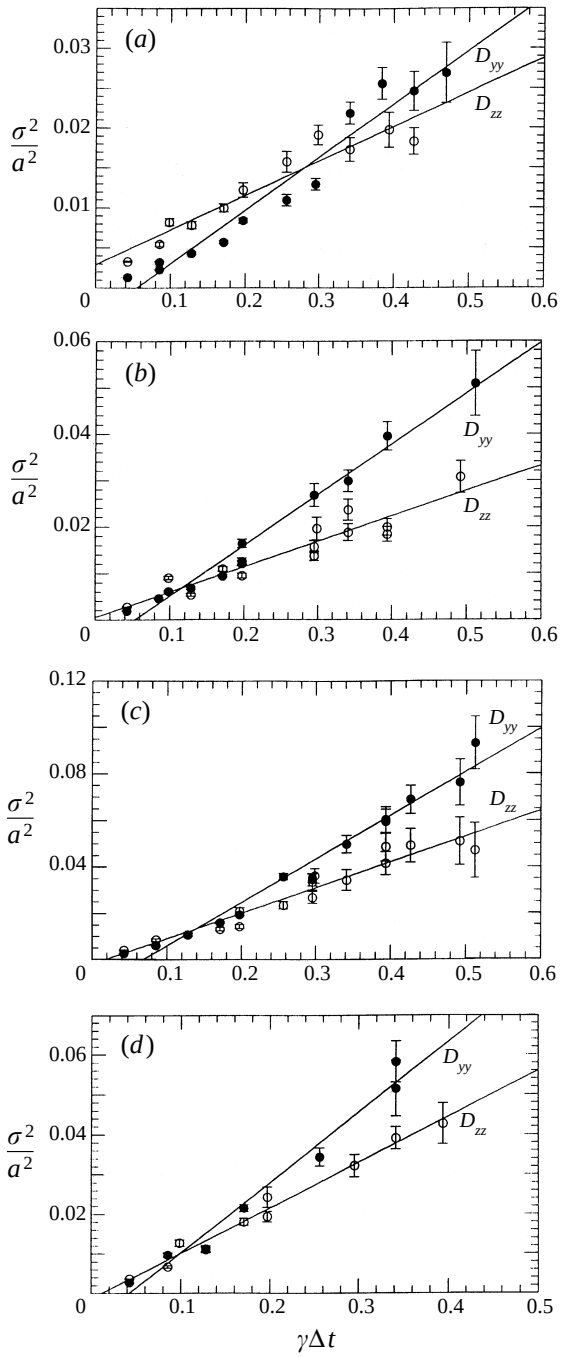

FIGURE 9. Plots of σ^2/a^2, the dimensionless variance of the correlation peak, vs. $\gamma\,\Delta t$ for (*a*) $\phi = 0.20$, (*b*) 0.30, (*c*) 0.40, (*d*) 0.50; the figures show the results for both the velocity gradient (•) and vorticity directions (○).

must be noted that although the width of the peak is small compared to the particle size, a clear broadening can be observed in going from figure 8(*a*) to 8(*b*), where Δt is increased.

The decrease in the peak height with increasing values of $\gamma\,\Delta t$ also limits the range

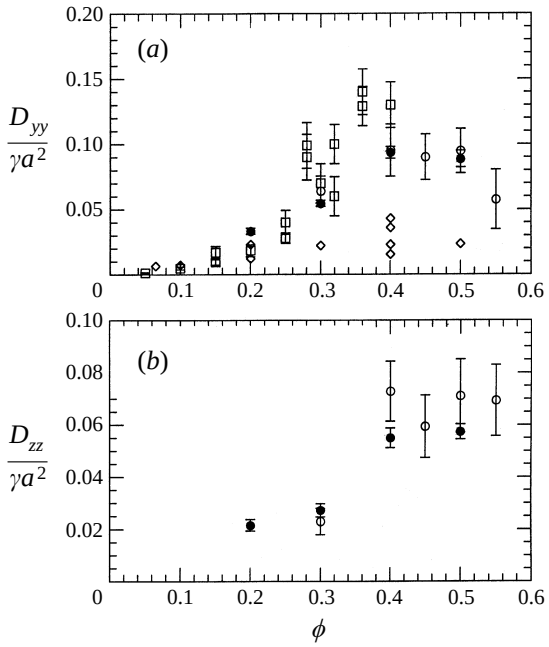

FIGURE 10. Comparison of the present results with previous experimental data for (*a*) the velocity gradient direction and (*b*) the vorticity direction. ○, from Phan & Leighton (1993): □, from Leighton & Acrivos (1987); ◇, from Eckstein *et al.* (1977); ●, from this study.

over which experiments could be performed, because the auto-correlation peak has to be distinguishable from the cross-correlation contribution. In our experimental set-up, measurements could be carried out for $\gamma\,\Delta t$ ranging from 0.05 to 0.5. For larger $\gamma\,\Delta t$ the particles did not remain within the window long enough to be detected in two consecutive images and thus contribute to the peak. This limitation was mainly caused by the fact that the experiments had to be performed in a region far enough from the wall of the outer cylinder to reduce wall effects as far as possible. The result is of a trade-off between the need to stay away from the wall and maximizing the range of $\gamma\,\Delta t$.

The width of the peaks in figure 8 is equal to the parameter σ_z defined in equation (2.9): $\sigma_z^2 = 2\,D_{zz}\,\Delta t$. For further analysis of the diffusion coefficient D_{zz} (and D_{yy}) and comparison with the results of other studies, the dimensionless scaling $\hat{D} = D/\gamma a^2$ must be introduced, where a is the particle radius. Using this formulation we therefore introduce the following two dimensionless diffusion coefficients:

$$\frac{\sigma_i^2}{a^2} = 2\,D_{ii}\,\gamma\,\Delta t, \quad i = y, z. \tag{4.1}$$

For all experiments, the width of the peak has been determined and the results are presented in figure 9(*a–d*) where the dimensionless values σ_y^2/a^2 and σ_z^2/a^2 are plotted versus $\gamma\,\Delta t$ for the different volume fractions. These figures show that the linear scaling of equation (4.1) applies over almost the entire range of $\gamma\,\Delta t$, i.e. from $\gamma\,\Delta t = 0.05$ to 0.5, although for $\phi = 0.20$ the linearity is not as clear as for the other experiments because the width of the auto-correlation peak is small and hence cannot be determined with much accuracy. The particle motion can, therefore, be described as a diffusive process on this time scale and the diffusive character seems to exist over

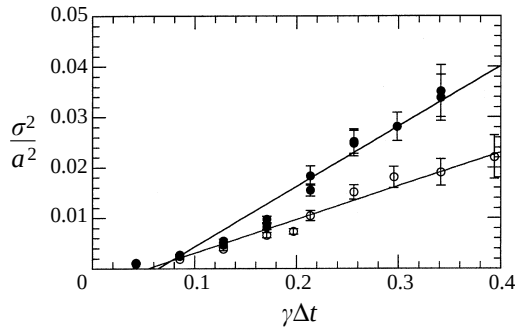

FIGURE 11. Plot of σ^2/a^2, the dimensionless variance of the correlation peak, vs. $\gamma\,\Delta t$ for $\phi = 0.40$; the figure shows the results for both the velocity gradient (•) and vorticity directions (○). This figure pertains to the fluid diffusivity experiments.

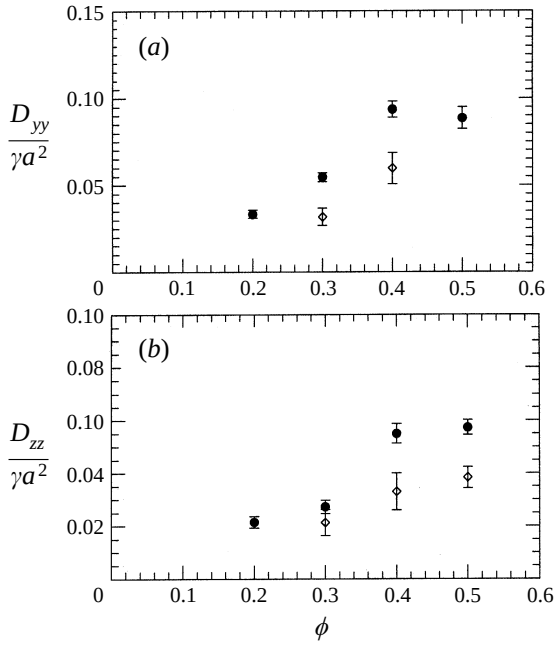

FIGURE 12. Comparison of the fluid and particle tracer diffusivity experimental data for (*a*) the velocity gradient direction and (*b*) the vorticity direction: ◇, fluid tracer diffusivity; •, particle self-diffusivity.

the entire range. This is rather surprising, because it was generally believed thus far that diffusive behaviour could only be attained for experimental time scales $\gamma\,\Delta t > 1$, i.e. when the time scales are larger than the assumed collision time in a simple shear flow and a particle has experienced several interactions.

Following equation (4.1), the dimensionless diffusion coefficients $\hat{D}_{yy}$ and $\hat{D}_{zz}$ can be calculated as one half the slope of the linear fits shown in figure 9(*a–d*). In all these figures, the diffusion coefficient in the velocity gradient direction ($\hat{D}_{yy}$) is considerably larger than in the vorticity direction ($\hat{D}_{yy}$) with the ratio being about 1.7 for all volume fractions.

Our results for the diffusion coefficients are plotted in figure 10(*a*, *b*) together with

the results of the previous studies by Eckstein *et al.* (1977), Leighton & Acrivos (1987*a*) and Phan & Leighton (1993). Although these earlier experiments were performed for $\gamma \Delta t \gg 1$ by measuring the transit time and position of single tracer particles, they are in remarkable agreement with our results for which $\gamma \Delta t < 1$. The error bars drawn for our data represent the uncertainty in the linear fits of figure 9(*a–d*) this error turned out to be dominant over the systematic errors, which were discussed in the previous section.

The self-diffusion coefficients $\hat{D}_{yy}$ and $\hat{D}_{zz}$ increase rapidly with increasing particle concentration, as was reported in all previous experimental studies, but their values appear to asymptote at $\phi = 50\%$. The same trend was also observed in the experiments by Phan & Leighton (1993).

4.3. *Fluid tracer diffusion in concentrated suspensions*

The fluid-diffusion coefficients were estimated by examining the motion of small tracers (31.5 ± 6.5 μm in diameter) within a concentrated suspension of 325 ± 25 μm diameter particles having concentrations ranging from 30% to 50% and for values of $\gamma \Delta t$ ranging from 0.1 to 0.4. It is assumed that the motion of these tiny tracers represented the true fluid element motion in a suspension of large particles. Following the method described in § 4.2, the dimensionless fluid tracer diffusivities D^f_{yy} and D^f_{zz} are calculated as one half the slope of the linear fits in plots of the dimensionless variance of the correlation peak vs. $\gamma \Delta t$. In figure 11, we present one such plot for $\phi = 0.40$ in both the velocity gradient and vorticity directions. Our results for the fluid diffusion coefficients are plotted in figures 12(*a*) and 12(*b*) together with the results of the particle diffusivities reported earlier in figures 10(*a*) and 10(*b*). Note that the diffusivities are scaled with γa^2, where a is the radius of particles making up the suspension. Unfortunately, measurements in the velocity gradient direction could not be performed for the case $\phi = 0.5$ due to the existence of a significant curvature in the interface between the suspension and the air above it. Clearly, the fluid tracer diffusion coefficients are about 0.7 times the corresponding particle diffusion coefficients.

The work described in this paper was supported in part by the Foundation for Fundamental Research on Matter (FOM) in the Netherlands and by the US Department of Energy under Grant No. DE-FG02-90ER14139A008. We would also like to thank Professor J. F. Brady for his useful comments and for providing the original of the first figure.

REFERENCES

Bossis, G. & Brady, J. F. 1987 Self-diffusion of Brownian particles in concentrated suspensions under shear. *J. Chem. Phys.* **87**, 5437–5448.

Brady, J. F. 1997 Shear-induced diffusion and particle migration. Presented at the AIChE Annual Meeting 1997, session 29D, Los Angeles.

Brady, J. F. & Morris, J. F. 1997 Microstructure of strongly sheared suspensions and its impact on rheology and diffusion. *J. Fluid Mech.* **348**, 103–139.

Eckstein, E. C., Bailey, D. G. & Shapiro, A. H. 1977 Self-diffusion of particles in shear flow of a suspension. *J. Fluid Mech.* **79**, 191–208.

Kampen, N. G. van 1992 *Stochastic Processes in Physics and Chemistry*, chap. VIII, pp. 210–212. Elsevier.

Krishnan, G. P., Beimfohr, S. & Leighton, D. T. 1996 Shear-induced radial segregation in bidisperse suspensions. *J. Fluid Mech.* **321**, 71–393.

Leighton, D. T. & Acrivos, A. 1987*a* Measurement of shear-induced self-diffusion in concentrated suspensions of spheres. *J. Fluid Mech.* **177**, 109–131.

Leighton, D. T. & Acrivos, A. 1987*b* The shear-induced migration of particles in concentrated suspensions. *J. Fluid Mech.* **181**, 415–439.

Phan, S. E. & Leighton, D. T. 1993 Measurement of the shear-induced tracer diffusivity in concentrated suspensions. *J. Fluid Mech.*, submitted.

Phung, T. 1993 Behavior of concentrated colloidal suspensions by Stokesian Dynamics simulation. PhD thesis, Californian Institute of Technology.

Phung, T., Brady, J. F. & Bossis, G. 1996 Stokesian Dynamics simulation of Brownian suspensions. *J. Fluid Mech.* **313**, 181–207.

Yurkovetsky, Y. 1998 I. Statistical mechanics of bubbly liquids; II. Behavior of sheared suspensions of non-Brownian particles. PhD thesis, Californian Institute of Technology.

Zydney, A. L. & Colton, C. K. 1988 Augmented solute transport in the shear flow of a concentrated suspension. *Physico Chem. Hydrodyn.* **10**, 77–96.